



## Letter

# Direct transfer patterning on three dimensionally deformed surfaces at micrometer resolutions and its application to hemispherical focal plane detector arrays

Xin Xu <sup>a,b</sup>, Marcelo Davanco <sup>b</sup>, Xiangfei Qi <sup>b</sup>, Stephen R. Forrest <sup>b,c,\*</sup>

<sup>a</sup> Department of Electrical Engineering, Princeton University, Princeton, NJ 08544, USA

<sup>b</sup> Department of Physics, University of Michigan, Ann Arbor, MI 48109, USA

<sup>c</sup> Departments of Electrical Engineering and Computer Science, and Materials Science and Engineering, University of Michigan, Ann Arbor, MI 48109, USA

## ARTICLE INFO

## Article history:

Received 16 July 2008

Accepted 16 July 2008

Available online 13 August 2008

## Keywords:

Three-dimensional

Cold welding

Focal plane array

Organic photodetector

## ABSTRACT

Formation of high performance organic electronic devices on three dimensionally deformed surfaces is severely constrained by the tensile stresses and shear that are introduced during the deformation process. Here, we overcome these limitations to demonstrate the direct transfer of unstrained metals via cold welding onto preformed, 1.0 cm radius plastic hemispheres with micrometer scale feature resolutions to realize 10 kilopixel organic photodetector focal plane arrays (FPAs) that mimic the size, function, and architecture of the human eye. The passive matrix FPA consists of  $(40\ \mu\text{m})^2$  organic double heterojunction photodetectors with response extending across the visible spectrum. The detector dark current density is  $5.3 \pm 0.2\ \mu\text{A}/\text{cm}^2$  at  $-1\ \text{V}$  bias, and with a peak external quantum efficiency of  $12.6 \pm 0.3\%$  at a wavelength of 640 nm. The photodetector impulse response was  $20 \pm 2\ \text{ns}$ , making the FPA suitable for video recording applications. The measured dynamic range allows for 7 bit image resolution, and the FPA is used to create a simple image. This demonstration significantly extends the ability to transfer active electronic devices that has previously only been demonstrated on planar substrates.

© 2008 Published by Elsevier B.V.

The approximately spherical human eye provides a nearly ideal imaging system: it is compact and simple, it has a very wide field of view (FOV) free of image distortion, and has a very low  $f/\text{number}$  [1] due to use of only a single lens element. This is in comparison to modern camera systems that employ multiple, high  $f/\text{number}$  lens elements to create a distortion-free image on a flat focal or film plane. This complex imaging system adds weight while limiting the FOV in the absence of fish-eye or other undesirable image aberrations [2]. To create an imaging system that mimics the form and function of the eye requires the

fabrication of a focal plane onto a nearly spherical surface that matches the curvature of a single lens element. Achievement of such an ambitious goal has long been sought by researchers interested in imaging systems [3–4], but it has been hampered by the need to create a high density of monolithically integrated photodetectors with micron scale dimensions on a 3 dimensionally curved surface. Here, we overcome these challenges by adapting processes for direct transfer of materials on planar surfaces to fabricate photodetector arrays onto preformed, 1.0 cm radius transparent plastic hemispheres with micrometer scale feature resolutions. We demonstrate a 10 kilopixel organic photodetector passive focal plane array (FPA) that mimics the size and architecture of the human eye. The passive matrix FPA consists of  $(40\ \mu\text{m})^2$  organic double heterojunction photodetectors with response extending across the visible spectrum.

\* Corresponding author. Address: Department of Physics, University of Michigan, Ann Arbor, MI 48109, USA.

E-mail addresses: [stevefor@umich.edu](mailto:stevefor@umich.edu), [dbeneven@princeton.edu](mailto:dbeneven@princeton.edu) (S.R. Forrest).

Two principal routes exist for the fabrication of monolithically integrated electronic circuits on arbitrarily shaped surfaces. One involves the patterning of circuits on a flat substrate, followed by deformation into its final shape [5]. This approach allows for the use of well-established patterning techniques prior to substrate deformation. Excessive strain during the deformation process may, however, cause damage to the various device layers, limiting its applicability to a narrow class of materials, and to surfaces with only limited deformation [5]. An alternative approach involves patterning directly on a pre-shaped substrate, such that the circuits are not subject to deformation-induced strain. This latter route is attractive because it allows for the realization of high performance devices over a nearly unlimited range of surface geometries. However, it presumes the availability of reliable patterning techniques for three-dimensional (3D) surfaces. Although various techniques for the generation of textured or patterned 3D surfaces have been reported [6–11], none have been used for the full realization of conformal electronics on nonplanar substrates. A combination of these two approaches includes partial fabrication of the circuit on a flat surface, followed by moderate deformation into its final 3D shape, at which point the fabrication is completed [12]. This typically employs wet chemical processing and conventional photolithography that are

incompatible with a range of semiconductor materials and substrates.

Here, we demonstrate a material transfer technique employing elastomeric stamps and cold welding [13–15] that allows for the definition of unstrained metallic patterns directly on top of curved surfaces covered with organic semiconductor materials. This allows for the fabrication of an organic, passive matrix focal plane array (FPA) on top of a 1.0 cm radius plastic hemisphere, depicted schematically in Fig. 1a. In contrast to similar, previously reported direct 3D material transfer methods [11,16–19], our technique is compatible with the realization of high performance monolithically integrated circuits composed of organic optoelectronic devices on arbitrarily deformed substrates, requiring no wet chemistry or high processing temperatures.

The passive matrix FPA consists of two perpendicular electrode stripe arrays placed above and below continuous layers of organic semiconductor materials forming the active photodetection regions. Individual photodetectors are defined at crossings of the upper and lower stripes, where device readout is realized by probing the appropriate row and column electrodes. Fig. 1b shows an example of a completed hemispherical FPA consisting of  $(500\text{ }\mu\text{m})^2$  copper phthalocyanine (CuPc)/C<sub>60</sub> based double heterojunction photodiodes.

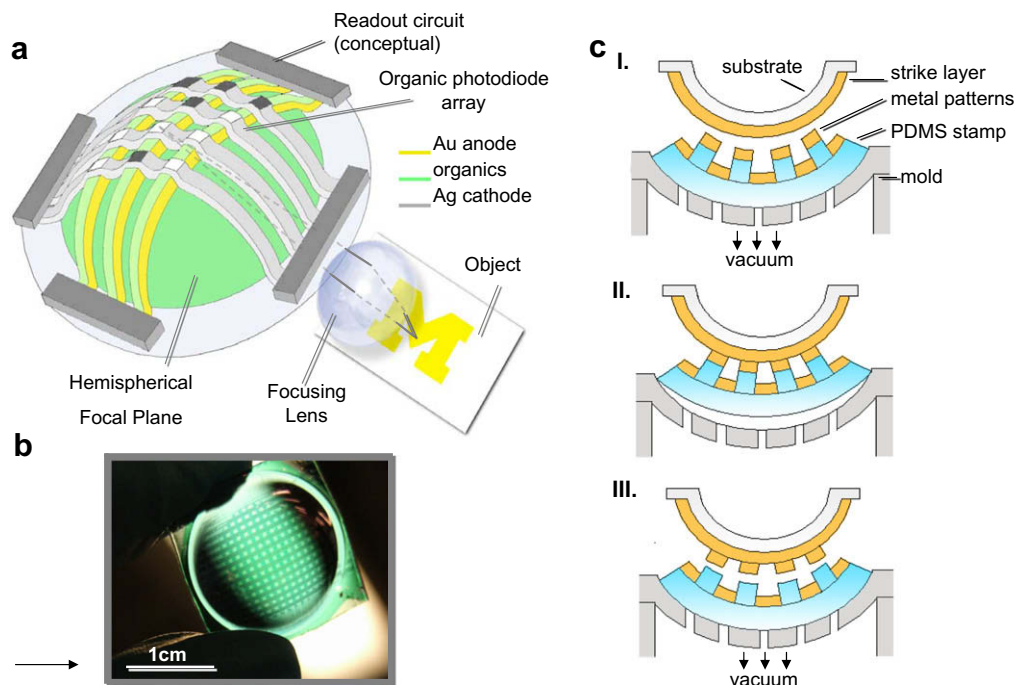


**Fig. 1.** (a) Schematic of the hemispherical organic photodetector focal plane array (FPA) and its incorporation into a simple imaging system. The lens produces an image of the object on the spherical focal plane, where an array of photodiodes has been defined. The readout circuits are commonly used in FPAs, but are not employed in our work. (b) Photograph of a completed hemispherical focal plane with a  $11 \times 13$  array of  $(500\text{ }\mu\text{m})^2$  photodetectors on a 1 cm radius plastic hemisphere fabricated following the process in Fig. 1c. (c) Process sequence for fabricating a hemispherical FPA. (c-I) The hemispherical plastic substrate, coated initially with a metal strike layer, is placed in proximity to a patterned PDMS stamp of the same shape, deformed by vacuum in an aluminum mold. (c-II) The vacuum holding the PDMS stamp is released, allowing the stamp to snap into contact with the substrate surface. Metallic bonds are formed between metal patterns on the stamp and strike layer on the plastic dome. (c-III) The PDMS stamp is separated from the substrate by re-application of vacuum, leaving behind the metal patterns on the hemisphere.

The fabrication process of the FPA shown schematically in Fig. 1c proceeds as follows: A flat and transparent, glycol-modified polyethylene terephthalate (PETg) sheet is drawn by vacuum into a shaped Al mold, while being heated to 140 °C above its softening temperature. The mold is then cooled to freeze the substrate shape. Next, a 2 nm Cr adhesion layer, and a 6 nm Au strike layer are thermally deposited onto the outer surface of the hemisphere in vacuum.

A flat PDMS stamp with an array of raised ridges that corresponds to the positions of the metal columns on the FPA is fabricated using a pre-etched Si “master” consisting of an array of parallel, 40  $\mu\text{m}$  or 500  $\mu\text{m}$  wide by 15  $\mu\text{m}$  high ridges, each separated by a distance equal to their widths [14–15]. Masters composed of a rigid material such as Si were patterned with lines of 40  $\mu\text{m}$  feature size using conventional photolithography. A curing agent and PDMS prepolymer were thoroughly mixed at a 1:7 weight ratio, followed by degassing for 1 h to remove all air bubbles and to ensure complete mixing. The prepolymer is then poured onto the Si master and cured at 100 °C for 1 h to form a stamp with duplicated patterns from the master.

The stamp is coated with a 10 nm thick Au layer by vacuum thermal evaporation, and then is also deformed into a hemispherical shape by applying vacuum to its flat surface, using the same mold as before. The spherical substrate is placed onto the mold in close proximity to the deformed PDMS stamp. The vacuum is then released, causing the PDMS stamp to “snap” back onto the substrate, conformal-

ly contacting its surface, as shown in Fig. 1c. A bond is thereby formed between the metal-coated ridges on the stamp and the strike layer. The PDMS stamp is parted from the substrate through re-application of the vacuum, leaving behind the metal stripes. The strike layer is then removed by sputtering in a 30 sccm, 20 Torr and 100 W Argon plasma etching for 2 min.

Following the transfer of the bottom (anode) electrode rows, organic semiconductor layers forming the diode active region are evaporated across the full surface of the hemisphere. The double heterojunction photodetectors consisted of a 50 nm thick CuPc donor layer, a 50 nm thick C<sub>60</sub> acceptor layer, a 10 nm thick bathocuproine (BCP) exciton blocking layer, and a 6 nm thick Ag strike layer grown sequentially by vacuum thermal evaporation. Finally, the top array of 20 nm thick Ag cathode columns are applied by a second, similar stamping process oriented perpendicularly to the first array of metal rows. The strike layer and the underlying organic semiconductors were then once again by exposure to an Ar plasma.

Using this process, Au or Ag stripes of thicknesses of up to 20 nm were transferred onto a 1 cm-radius hemisphere (Fig. 2a and b). Transfer of thicker metals proved to be difficult, possibly due to wrinkling of the PDMS stamp during metal deposition [21].

Fig. 2a shows an array of 10 nm thick, 500  $\mu\text{m}$  wide Au stripes transferred onto a PETg hemisphere. A sheet resistance of 7  $\Omega/\square$  for 10 nm Au was estimated from measurements made between several points along the metal

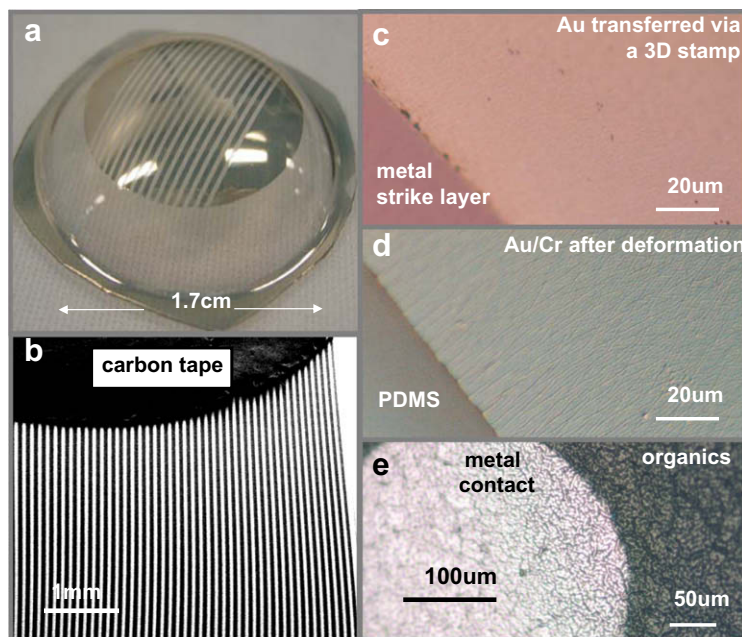


**Fig. 2.** (a) Optical microscope image of a 500  $\mu\text{m}$  wide, cm-long and 10 nm thick Au stripe array on a PETg hemisphere produced with the process in Fig. 1c. (b) Scanning electron microscope image of an array of 40  $\mu\text{m}$  wide metal stripes patterned on a hemispherically shaped substrate. The distortion of the stripe patterns at the edge of the substrate results from the PDMS stamp deformation illustrated in Fig. 1c. (c) Optical microscope image showing the edge of a metal stripe patterned via the direct material transfer illustrated in Fig. 1c, before Ar plasma etch. (d) Microscope image of Au film with a 20 Å Cr as an adhesive layer on PDMS after deforming into a 1 cm radius hemisphere. Cracking is apparent after same strain is applied as compared to Fig. 2c due to increased adhesion between metal film and PDMS. (e) Microscope image showing cracks on both metal and organic layers predeposited on a flat plastic substrate, followed by deformation to the same degree as in (c) and (d).

stripes. This corresponds to  $7 \times 10^{-6} \Omega \text{ cm}$ , consistent with that of conventional Au thin films. Since the stripe layer thickness is the same as that of the transferred lines, significant fracturing of the transferred metal would lead to discontinuous electrodes created during the Ar etch, which is clearly not observed.

In Fig. 2b, we show a distortion of  $40 \mu\text{m}$  wide stripe patterns along the edge of the interconnect array due to 3D deformation of the parallel stripes on the planar stamp. If desired, this distortion can be corrected by modifications to the stamp pattern. The edge features of the  $40 \mu\text{m}$  metal stripes have a roughness of  $1\text{--}2 \mu\text{m}$ , suggesting that pattern resolutions  $<10 \mu\text{m}$  are achievable.

The strain introduced on the PDMS stamp (or plastic substrate) during deformation is a function of the radius of curvature [6]. The average strain for a full hemisphere as demonstrated here, is approximately 20%, being slightly higher at the apex than at the rim. Given that free-standing metal films fracture at strains of only a few percent [22–

23], the high quality metal pattern transfer suggests that significant shear slip occurs at the metal/PDMS interface during stamp deformation, due to the weak adhesion at the Au/PDMS interface. As shown in Fig. 2c, 10 nm thick Au stripe transferred by a 3D stamp shows no metal cracking. If the adhesion between metal film and PDMS is enhanced, for example, by inserting a 2 nm thick Cr adhesive layer (Fig. 2d), the metal film can not be transferred and cracks under the same amount of strain as in Fig. 2c [23]. In Fig. 2e, we show that metal contacts deposited onto plastic substrates prior to deformation also leads to significant cracking of both organic and metallic layers due to the strong metal/PETg bond that inhibits shear-induced slip.

Following the transfer of the bottom (anode) electrode rows, organic semiconductor layers forming the double heterojunction copper phthalocyanine (CuPc)/ $\text{C}_{60}$  diode [20] active region are evaporated across the full surface of the hemisphere, followed by deposition of a 10 nm thick

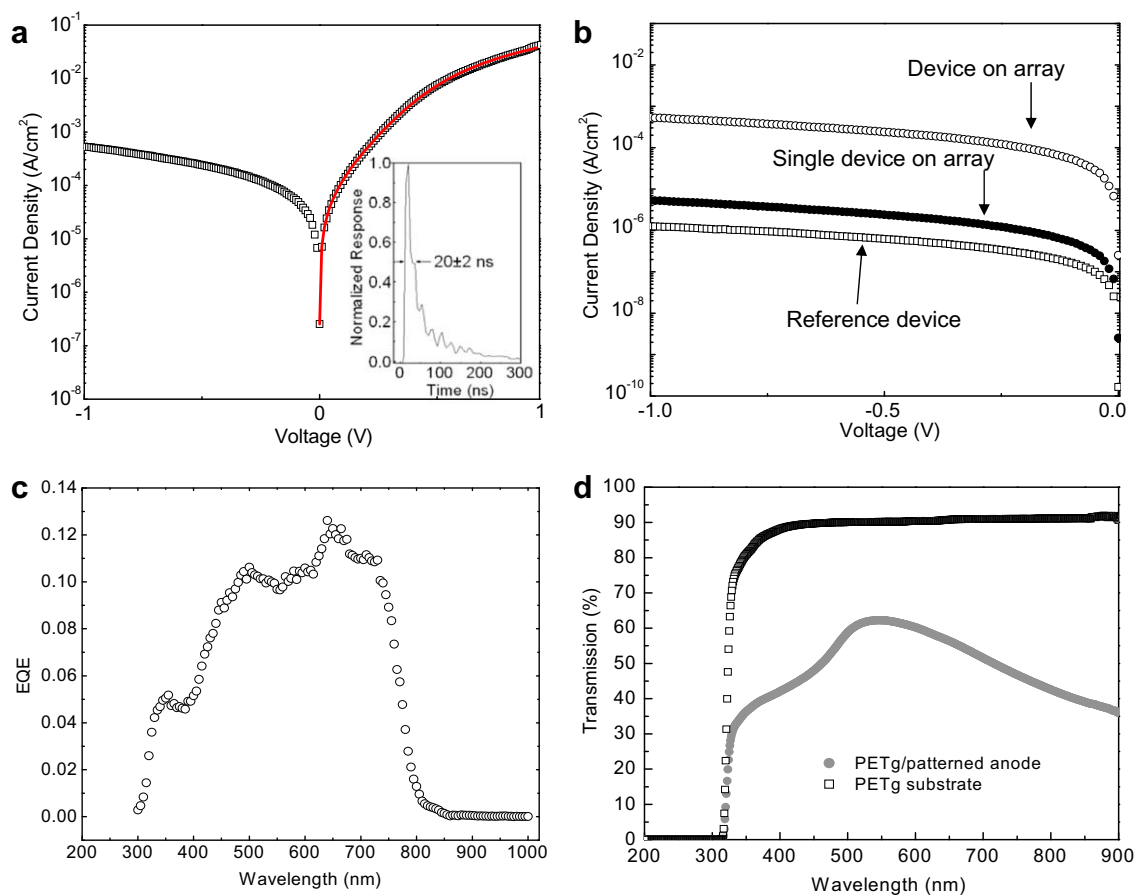


**Fig. 3.** (a) Current density–voltage characteristics for an individual  $(40 \mu\text{m})^2$  organic photodetector under forward and reverse bias. The data at  $<0.5 \text{ V}$  forward bias was fit (solid line) using the modified Shockley equation,  $J = J_s \cdot \exp[(qV - JR_{sa})/n'kT]$ , where the specific series resistance  $R_{sa} = 0.33 \pm 0.01 \Omega \text{ cm}^2$ , saturation current density  $J_s = (60 \pm 2) \mu\text{A cm}^{-2}$  and  $n' = 3.49 \pm 0.03$  are used. Note that  $n' > 2$  results since the current is summed over the reverse currents of several diodes in the passive matrix array, and is thus affected by the sum of their resistances. *Inset:* Pulse response of a  $(40 \mu\text{m})^2$  photodetector on the hemispherical array, showing a response time of  $20 \pm 2 \text{ ns}$ . (b) Total dark current density under reverse bias (open circles), and estimated dark current of a  $40 \mu\text{m}$  detector (closed circles) in a  $100 \times 100$  focal plane array. The reverse biased dark current density of a device on a flat substrate (open squares) is shown for comparison. (c) External quantum efficiency of a transferred detector (1 mm in diameter) at 0 V bias. (d) Transmission spectrum of the PETg substrate with and without a  $100 \text{ \AA}$  patterned Au anode array.



Ag strike layer. Finally, the top array of 20 nm thick Ag cathode columns are applied by a second, similar stamping process oriented perpendicularly to the first array of metal rows.

Electrical characterization of individual pixels was performed on the  $100 \times 100$  array of  $(40 \mu\text{m})^2$  photodetectors fabricated on a 1 cm radius hemispherical substrate. Photodetector dark currents measured along a row or column yielded a total current density of  $530 \pm 20 \mu\text{A cm}^{-2}$  at  $-1 \text{ V}$  (Fig. 3a), which is approximately 100 times greater than for an individual diode. The dark current density for an isolated device is thus less than or equal to  $5.3 \pm 0.2 \mu\text{A cm}^{-2}$ , which is comparable to that measured for an analogous, 1 mm-diameter control device on a flat glass/ITO substrate, as shown in of Fig. 3b.

The external quantum efficiency, shown in Fig. 3c, is  $>10\%$  for wavelengths between  $\lambda = 480 \text{ nm}$  to  $740 \text{ nm}$ , peaking at  $12.6 \pm 0.3\%$  at  $\lambda = 640 \text{ nm}$ . As shown in Fig. 3d, transmission through the 10 nm thick Au layer on PETg is 60% at  $\lambda = 640 \text{ nm}$ , leading to a decrease of external quantum efficiency compared to previously reported CuPc/C<sub>60</sub>/BCP double heterojunction photodetectors [20]. Given the reflection from the metal cathode, absorption of both metal contacts, and a calculated absorption of the organic donor/acceptor layers of 40% at  $\lambda = 640 \text{ nm}$  [24], the internal quantum efficiency is approximately 30%. This is lower than previously reported [24] due to the thick CuPc layer used to reduce the possibility of electrical shorts between top and bottom electrodes. This, in turn, reduces the exciton diffusion efficiency, and hence the internal quantum efficiency.

The photodetector noise performance may be evaluated by determination of the detectivity  $D^* = (A\Delta f)^{1/2}/\text{NEP}$ , where  $A$  is the detector area,  $\Delta f$  is the bandwidth, and NEP is the noise equivalent power [25]. In our case, shot noise limited detection at  $-1 \text{ V}$  gives,  $\text{NEP} = (2qI_D)^{1/2}/R(\lambda)$ , where  $q$  is the electronic charge,  $I_D$  is the dark current, and  $R(\lambda)$  is the detector responsivity. At  $\lambda = 640 \text{ nm}$ , we obtain  $R = 0.065 \text{ AW}^{-1}$ . In this case,  $D^* = 5 \times 10^{10} \text{ cm}^2 \text{ W}^{-1} \text{ Hz}^{-1/2}$  in a 1 Hz bandwidth, which is approximately ten times less than that of a Si photodiode [26].

The current density vs. voltage characteristics of 100 pixels were measured over four different regions on the 1 cm hemisphere. None of the 100 devices was found to be electrically shorted. Indeed, devices in the center and near the edge of the matrix show less than 10% variation in average dark current, possibly due to variations in layer thickness across the hemispherical surface. This residual non-uniformity can be minimized by substrate rotation during material deposition. Among all devices, 97% have dark current densities  $<20 \mu\text{A cm}^{-2}$  at  $-1 \text{ V}$ .

The temporal response of a photodetector in the array to an optical pulse shown in the inset of Fig. 3a, was  $(20 \pm 2) \text{ ns}$ . The response was characterized by illumination with a 5 Hz train of 700 ps full width at have maximum (FWHM) pulses at  $\lambda = 475 \text{ nm}$  from a dye pumped with a  $\text{N}_2$  laser. The average optical power was  $0.29 \pm 0.02 \mu\text{J}$  over a 5 mm diameter illuminated spot. The response is limited by the detector resistance and capacitance, where a series resistance of approximately 20 k $\Omega$ , is estimated from the forward-biased current den-

sity vs. voltage characteristic in Fig. 3a (solid line), and the capacitance measured at 10 kHz was  $1.31 \pm 0.01 \text{ pF}$ . The response time is compatible with pixel readout rates of  $\sim 10^7$  pixels/s, which translates into a frame readout rate in excess of the 30 frames per second video standard for a  $640 \times 480$  pixel array. Real-time imaging applications are thus achievable with this architecture.

To demonstrate the imaging capabilities of hemispherical FPAs, we fabricated a  $20 \times 20$  array of  $(200 \mu\text{m})^2$  pixels spaced by  $300 \mu\text{m}$  on a 1 cm radius hemisphere, a configuration that facilitated probing and readout. The detector dynamic range was extracted by measuring the photocurrent of a single device under different illumination levels at  $\lambda = 633 \text{ nm}$  and three different bias voltages, as shown Fig. 4. Fits to the data are shown as solid lines, indicating approximately linear photocurrent variation with optical power in the range of 2 to  $200 \mu\text{W cm}^{-2}$ . Photocurrent compression with respect to the linear fits is observed at high optical powers, while at very low optical powers, the photocurrent is noise limited, evidenced by the error bars. Note that the increasing y-axis intercept with increasing reverse bias corresponds to a larger responsivity. The dynamic range (DR) is defined as  $10\log(P_1/P_0)$ , where  $P_1$  is the optical power for 1 dB photocurrent compression at high intensities, and  $P_0$  is the lowest detectable optical power. For 0 V bias, DR = 20 dB, corresponding to a 7-bit gray-scale. At higher reverse bias, the 1 dB compression point exceeds the highest input power while  $P_0$  remains the same. The increased linearity, therefore, leads to an increased DR due to the space charge field that sweeps out more free carriers at high intensity.

To demonstrate imaging capabilities, a rectangular, a  $1.3 \times 0.8 \text{ mm}^2$  aperture placed in proximity to the hemispherical center line, was illuminated at  $\lambda = 633 \text{ nm}$  at

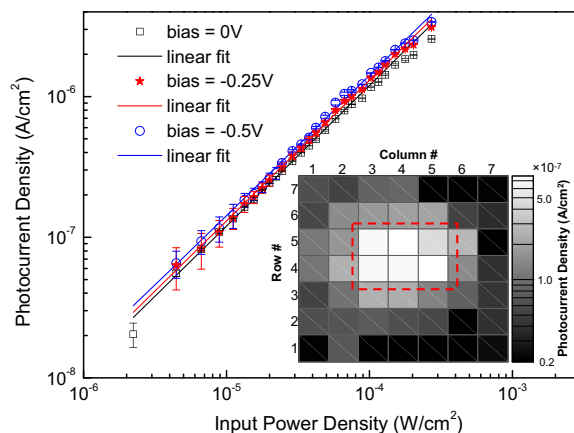


**Fig. 4.** Photocurrent density vs. input power density of a  $(200 \mu\text{m})^2$  photodetector in a  $20 \times 20$  array under various biases. Linear fits at each bias are shown as solid lines. The dynamic range, determined by the 1 dB compression point and minimum detectable power level, is approximately 20 dB, giving a 7-bit resolution. Inset: Gray scale image of a rectangular illuminated area on the hemispherical FPA, corresponding to a  $2 \times 3$  block of photodetectors. Photocurrents of all pixels in a  $7 \times 7$  block containing the illuminated block are depicted, showing high contrast obtained between illuminated and unilluminated pixels. Illumination was provided by a 633 nm laser beam.

$120 \mu\text{W cm}^{-2}$ . The illuminated area included a  $2 \times 3$  pixel block and portions of the immediately adjacent pixels. Photocurrents from pixels within a  $7 \times 7$  block including the illuminated area were measured and used to generate the 7-bit gray scale image in Fig. 4, inset. The dashed rectangle illustrates the approximate extent of the illuminated area. A contrast of 99% exists between the highest and lowest pixel photocurrents located, respectively, at the center and periphery of the block. A photocurrent non-uniformity of 13% is observed among pixels in the high-illumination  $2 \times 3$  pixel block, excluding the pixel at position (5,5). Gray levels at partially illuminated pixels on the periphery of the rectangle exhibit a minimum contrast of 71% with respect to the maximum photocurrent. The observed non-uniformities are due to imperfections in the imaging system, light leakage, scattering from metal contact surfaces, and slight variations in the individual pixel characteristics. Given low carrier mobility of vacuum-deposited organic semiconductor materials, low pixel electrical crosstalk is expected in this passive architecture.

In summary, we have demonstrated a direct material transfer technique that is adaptable to surfaces of arbitrary 3D shape. The technique avoids introduction of excessive strain into heterogeneous material layers, thus allowing for the fabrication of high performance organic electronic devices with micrometer scale dimensions on curved surfaces with radii 1 cm or less. The technique was applied to the fabrication of a lightweight and compact hemispherical FPA. Another interesting yet challenging application is the use of curved FPAs as retinal prostheses to replace photoreceptor cell layers that have degenerated and lost sensation to different shades of light.

## Acknowledgements

The authors thank the Defense Advanced Research Projects Agency, the Air Force Office of Scientific Research, the National Science Foundation and Universal Display Corporation for financial support. The authors also thank Stephanie Kena-Cohen and Noel Giebink for helpful discussions.

## References

- [1] In an optical imaging system, the  $f$ /number is defined as the focal length of the imaging lens divided by the diameter of the entrance aperture. Larger  $f$ -numbers express lesser amounts of light per unit area reaching the image plane. The largest observable angle of the optical system defines its FOV. See, for example E. Hecht, *Optics*, Addison Wesley, 2002.
- [2] R. Dinyari, S.-B. Rim, K. Huang, P.B. Catrysse, P. Peumans, *Appl. Phys. Lett.* 92 (2008).
- [3] I. Sample, *New Sci.* 170 (2001) 23.
- [4] W.J. Hamilton, P.R. Norton, E.E. Gordon, R.W. Berry, US Patent Number 6,627,865 B1, 2003.
- [5] R. Bhattacharya, S. Wagner, Y.-J. Tung, J.R. Esler, M. Hack, *Proc. IEEE* 93 (2005) 1273.
- [6] K.E. Paul, M. Prentiss, G.M. Whitesides, *Adv. Func. Mater.* 13 (2003) 259.
- [7] P. Ruchhoeft, M. Colburn, B. Choi, H. Nounu, S. Johnson, T. Bailey, S. Damle, M. Stewart, J. Ekerdt, S.V. Sreenivasan, J.C. Wolfe, C.G. Willson, *J. Vac. Sci. Technol. B* 17 (1999) 2965.
- [8] W.M. Choi, O.O. Park, *Nanotechnology* 15 (2004) 1767.
- [9] W.R. Childs, R.G. Nuzzo, *Adv. Mater.* 16 (2004) 1323.
- [10] K. Hashimoto, Y. Kaneko, T. Horiuchi, *Microelectron. Eng.* 83 (2006) 1312.
- [11] S.M. Miller, S.M. Troian, S. Wagner, *J. Vac. Sci. Technol. B* 20 (2002) 2320.
- [12] P.I. Hsu, R. Bhattacharya, H. Gleskova, M. Huang, Z. Xi, Z. Suo, S. Wagner, J.C. Sturm, *Appl. Phys. Lett.* 81 (2002) 1723.
- [13] C. Kim, P.E. Burrows, S.R. Forrest, *Science* 288 (2000) 831.
- [14] C. Kim, M. Shtein, S.R. Forrest, *Appl. Phys. Lett.* 80 (2002) 4051.
- [15] C. Kim, S.R. Forrest, *Adv. Mater.* 15 (2003) 541.
- [16] G.S. Ferguson, M.K. Chaudhury, G.B. Sigal, G.M. Whitesides, *Science* 253 (1991) 776.
- [17] Y. Xia, G.M. Whitesides, *Angew. Chem. Int. Ed.* 37 (1998) 550.
- [18] B. Michel, A. Bernard, A. Bietsch, E. Delamarche, M. Geissler, D. Juncker, H. Kind, J.P. Renault, H. Rothuizen, H. Schmid, P. Schmidt-Winkel, R. Stutz, H. Wolf, *IBM J. Res. Dev.* 45 (2001) 697.
- [19] H.O. Jacobs, G.M. Whitesides, *Science* 291 (2001) 1763.
- [20] P. Peumans, S.R. Forrest, *Appl. Phys. Lett.* 79 (2001) 126.
- [21] N. Bowden, S. Brittain, A.G. Evans, J.W. Hutchinson, G.M. Whitesides, *Nature* 393 (1998) 146.
- [22] P.H. Hsu, M. Huang, S. Wagner, Z. Suo, J.C. Sturm, *Mater. Res. Soc. Symp. Proc.* 621 (2000) Q8.6.1.
- [23] S.P. Lacour, J. Jones, S. Wagner, T. Li, Z. Suo, *Proc. IEEE* 93 (2005) 1459.
- [24] P. Peumans, A. Yakimov, S.R. Forrest, *J. Appl. Phys.* 93 (2003) 3693.
- [25] NEP corresponds to the optical power required to produce a unity signal-to-noise ratio at the detector output. Photodiode noise current consists of shot and thermal noise. Shot noise is dominant at sufficiently high reverse bias.
- [26] A. Rogalski, *Opto-Electron. Rev.* 12 (2004) 221.